JOURNAL OF GEOPHYSICAL RESEARCH, VOL. ???, XXXX, DOI:10.1029/,

On the Role Played by Magnetic Expansion Factor in the Prediction of Solar Wind Speed

Pete Riley[1] , Jon A. Linker[1], and C. Nick Arge[2]

Pete Riley and Jon A. Linker, Predictive Science, 9990 Mesa Rim Road, Suite 170, San Diego, CA, USA. (pete@predsci.com; linkerj@predsci.com)

C. Nick Arge, AFRL/Space Vehicles Directorate, Kirtland AFB, NM, USA. (AFRL.RVB.PA@kirtland.af.mil)

[1]Predictive Science, 9990 Mesa Rim Road, Suite 170, San Diego, CA 92121, USA.

[2]AFRL/Space Vehicles Directorate, Kirtland AFB, NM, USA.

Abstract. Over the last two decades, the Wang-Sheeley-Arge (WSA) Model has evolved significantly. Beginning as a simple observed correlation between the expansion factor of coronal magnetic field lines and the measured speed of the solar wind at 1 AU (the WS model), the WSA model now drives NOAA's first operational space weather model, providing real-time predictions of solar wind parameters in the vicinity of Earth. Here, we demonstrate that the WSA model has evolved so much that the role played by the expansion factor term is now largely minimal, being supplanted by the distance from the coronal hole boundary (DCHB). We illustrate why, and to what extent the three models (WS, DCHB, and WSA) differ. Under some conditions, all approaches are able to reproduce the grossest features of the observed quiet-time solar wind. However, we show that, in general, the DCHB- and WSA-driven models tend to produce better estimates of solar parameters at 1 AU than the WS model, particularly when pseudo-streamers are present. Additionally, we highlight that these empirical models are sensitive to the type and implementation of the magnetic field model used: In particular, the WS model can only reproduce in situ measurements when coupled with the PFSS model. While this clarification is important both in its own right and from an operational/predictive standpoint, because of the underlying physical ideas upon which the WS and DCHB models rest, these results provide support, albeit tentatively, for boundary-layer theories for the origin of the slow solar wind.

1. Introduction

The prediction of interplanetary magnetic field (**B**), velocity (**v**), and to a lesser extent, number density (n), and plasma temperature (T) in the vicinity of Earth is a crucial component of any future reliable space weather capability [e.g. *Pizzo et al.*, 2011]. Yet, understanding and reproducing the structure of the inner heliosphere, even in the absence of obviously time-dependent phenomena such as coronal mass ejections (CMEs) is a challenging task. Over the years, a variety of approaches to connect what is observed at the Sun with what is measured *in-situ* in the vicinity of Earth have been adopted, ranging from simple empirical relationships [e.g. *Wang and Sheeley*, 1990] to sophisticated global MHD models [e.g. *Riley et al.*, 2011]. Currently, the empirical models at least match, and arguably outperform the physics-based, first-principles models [*Owens et al.*, 2008b].

Global heliospheric models, such as WSA-Enlil [e.g. *Jian et al.*, 2011], and, more generally, CORHEL [*Riley et al.*, 2012a], produce time series of **B**, **v**, n, and T at 1 AU in two key steps. First, a synoptic map of the photospheric magnetic field is used as the primary driver of the coronal model, which may be a Potential Field Source Surface (PFSS) or MHD model [*Riley et al.*, 2006]. This component of the model typically spans the range from $1R_S$ to $2.5R_S$ (PFSS) or $20-30R_S$ (MHD). Second, the heliospheric domain ($20-30R_S$ to 1 AU) is driven either directly using results from the coronal model or indirectly by constructing boundary conditions based on the topology of the coronal magnetic field [*Riley et al.*, 2001]. Heliospheric boundary conditions derived from PFSS solutions at $2.5R_S$ are mapped outward without change to the inner boundary of the heliospheric model at $30R_S$.

In this study, we focus on these indirect techniques used to derive the boundary conditions, and particularly the solar wind speed, for the heliospheric model. Since the structure of the solar wind is dominated by the dynamic pressure term in the momentum equation ($\sim \rho v^2$), errors in determining the correct flow speed at the inner boundary of the heliospheric model have the most significant impact on the heliospheric solutions.

Currently, there are three principal empirical techniques in use for computing the large-scale properties of solar wind speed at some reference sphere (say, $30R_S$, beyond which the flow is radial). First, the original Wang-Sheeley (WS) model (Wang and Sheeley, 1990) uses an observed negative correlation between solar wind speed (at 1 AU) and the super-radial expansion factor of the solar magnetic field. Second, the "Distance from the Coronal Hole Boundary" (DCHB) model [*Riley et al.*, 2001] specifies speed at the photosphere based on the perpendicular distance from the coronal hole boundary and maps this speed out along field lines to $30R_S$. Third, the Wang-Sheeley-Arge (WSA) model [*Arge et al.*, 2003], which, although considered to be a refinement to the WS model, in fact, combines terms capturing both the WS and DCHB effects [*Arge et al.*, 2004]. Our aim in this study is to identify the similarities and differences between these methods, understand why they arise, and perform parametric studies of these techniques to assess which model(s) produce(s) the best match with 1 AU measurements.

There remains confusion – or perhaps ambiguity – in the scientific community about the precise definition of the WS, DCHB, and WSA approaches. *Shiota et al.* [2014], for example modeled the global ambient structure of the inner heliosphere using what they defined as the WSA model. They employed, however, an early version of the WSA model that included only the expansion factor [*Arge and Pizzo*, 2000], and thus, should have been defined as a variant of the WS model, or perhaps more specifically as WSA-2000. In contrast, here we apply the most updated version of WSA, as defined by *Arge et al.* [2003, 2004].

It is worth noting that the DCHB model is distinct from approaches relying on the minimum angular distance from the heliospheric current sheet (HCS) [*Hakamada and Akasofu*, 1981], in which the wind speed is assumed to slow in a band within some angular minimum distance from the HCS, computed at some reference height (say $2.5R_S$ for PFSS models or $20-30R_S$ for MHD models) and fast everywhere else. In particular, the DCHB model specifies the slow wind along bands in the photosphere, adjacent to the open-closed field line boundaries, and the resulting speed profile is then mapped along field lines to some reference height. Only for highly idealized geometries, such as a tilted dipole field, would these approaches be expected to produce similar results. Phrased another way, the DCHB model describes the wind profile near its source, at the base of the corona, whereas a technique based on distance from the HCS attempts to describe the profile at some point of relative equilibrium. Comparisons of the WS model and a model based on the the angular distance from the HCS with *in-situ* measurements, showed that the latter resulted in substantially worse correlations with observations [*Wang and Sheeley*, 1997].

Previous studies that have assessed our ability to predict the bulk solar wind speed have revealed that models are only modestly, if at all, better than "persistence" [e.g. *Norquist and Meeks*, 2010], that is, that tomorrow's speed, say, will be the same as the current speed, "recurrence," where the prediction is based on observed values 27 days earlier [*Owens et al.*, 2013]. More recently, *Bussy-Virat and Ridley* [2014] developed a probability distribution function (PDF) model for predicting solar wind speed by combining a prediction based on the current value and gradient in solar wind speed as well as its value one rotation earlier. They argued that the PDF model outperformed the "persistence" model for predictions up to five days in the future (Pearson Correlation Coefficient, $PCC \sim 0.52$), and the WSA model for predictions < 24 hours in advance.

While the specification of solar wind speed at $30R_S$, as outlined here, is empirical, the prescriptions are linked to fundamentally different ideas on the origin of the slow solar wind [*Riley and Luhmann*, 2012]. Thus, in principle, it may be possible to derive some physical insight from comparisons of different empirical models. The WS model relies on the expansion factor of the local flux tube to govern the resulting speed, density, and temperature of the escaping solar wind. Detailed physics-based models have been developed that suggest that the incorporation of waves and turbulence, in conjunction with expansion factor may reproduce the basic properties of the slow and fast wind [*Cranmer*, 2010]. Other studies have argued that expansion factor may even be able to account for the unique compositional differences between slow and fast solar wind [*Laming*, 2004]. In contrast, the DCHB model prescribes slow solar wind adjacent to the boundary between open and closed field lines, and fast wind everywhere else, and is more closely linked to a "boundary layer" (BL) idea, such as "interchange reconnection," for the origin of the slow solar wind [*Wang et al.*, 1996; *Fisk*, 1996; *Antiochos et al.*, 2011], since it is at the boundary between the open and closed field lines, i.e., the coronal hole boundaries, where this reconnection is expected to take place. Thus, should either the WS or DCHB model perform significantly better than the other, this would provide support for the underlying physical mechanism.

In the sections that follow, we first describe these velocity map models, and then apply them to two specific Carrington rotations, 1913 and 2060. We perform a detailed parametric study for these rotations, which were relatively quiescent and have been well studied [e.g. *Riley et al.*, 1999; *Riley et al.*, 2012b]. Our goal here is not to firmly establish what the best-fit parameters are in each model, but rather to understand what factors drive the profiles that the models produce, and understand how the techniques are related to one another. Following this, we compute solutions for all rotations from September 1995 through August 2010 (CRs: 1900 - 2100), i.e., spanning more than a solar cycle, using a representative set of parameters for each model and compare the model results with *in-situ* measurements. We conduct this exercise using both MHD and PFSS model solutions. Finally, we draw some conclusions and suggest how future studies may build upon this work.

2. The Velocity Map Models

In this section, we summarize the main properties of the WS, DCHB, and WSA models. Since they rely on the concepts of expansion factor and the location of coronal hole (CH) boundaries, we also discuss the relationship of these parameters to one another, as well as to the location of the HCS. It is important to emphasize at the outset, that we are exploring different implementations of these models that capture their salient features. In particular, they cannot be referenced to specific versions of a particular model, since the models themselves have undergone gradual and continuous changes over the years. In fact, our parametric study aims at identifying an optimum set of parameters for each model, at least within the confines of this study.

2.1. The Wang-Sheeley Model

The WS model is based on the observation that the speed of the solar wind measured at 1 AU negatively correlates with magnetic flux tube expansion factor (f_s) nearer the Sun [*Wang and Sheeley*, 1990]. Although the WS model was initially determined purely from comparisons of f_s with measured solar wind at 1 AU, a theoretical explanation for why such a relationship should hold was subsequently developed [e.g. *Wang et al.*, 2009]. An important aspect of this idea is that the production of the slow solar wind does not require any reconnection to open previously closed field lines.

Following [*Wang and Sheeley*, 1997], we can write the areal expansion factor, f_s as:

$$f_s = \left(\frac{R_S}{R_1}\right)^2 \frac{B_r(R_S, \theta_o, \phi_o)}{B_r(R_1, \theta_1, \phi_1)} \tag{1}$$

This expression relates the amount by which a flux tube expands from one location (r_o, θ_o, ϕ_o), say at the solar surface ($r_o = R_S$) to another, usually higher in the corona (r_1,θ_1,ϕ_1), e.g., $2.5R_S$ for PFSS models and $20-30R_S$ for MHD models. We note that the expansion factor is above and beyond the field expansion that would occur for a monopole field ($f_s \sim 1/r^2$).

More generally, we can write the WS relationship as:

$$V_{WS}(f_s) = V_{slow} + \frac{(V_{fast} - V_{slow})}{(f_s)^\alpha} \tag{2}$$

where v_{slow} is the lowest solar wind speed expected as $f_s \to \infty$, v_{fast} is the fastest solar wind speed expected as $f_s \to 1$, and α is, in principle, some coefficient also to be determined *Arge and Pizzo* [2000]. Wang (Personal Communication, 2014) has advocated that a value of $\alpha = 1$ is appropriate. In this limit, equation 2 reduces to the original relationship proposed by *Wang and Sheeley* [1990]. Additionally, we also impose minimum and maximum speed limits of, say, 360, and 750 km/s (which could be free parameters) to account for the fact that this expression could potentially lead to speeds in excess of those observed by Ulysses for quiet solar wind conditions.

2.2. The "Distance from the Coronal Hole Boundary" Model

The DCHB model depends on the angular, minimum (perpendicular) distance from the coronal hole boundary to specify the solar wind speed [*Riley et al.*, 2001]. This is computed at the photosphere and the speeds are mapped along field lines to the reference sphere, $30R_S$, in this case. The DCHB model can be expressed as:

$$V_{DCHB}(d) = V_{slow} + \frac{1}{2}\left(V_{fast} - V_{slow}\right)\left(1 + \tanh\left(\frac{d - \epsilon}{w}\right)\right) \quad (3)$$

where d is the minimum, or perpendicular distance from an open-closed boundary, that is from a CH boundary, at the photosphere, ϵ is a measure of how thick the slow flow band is, and w is the width over which the flow is raised to coronal hole values [*Riley et al.*, 2001]. The parameters V_{slow} and V_{fast} are analogues (but, given the difference in formulation, likely to be different) to the same-named parameters in the WS model. At the boundary between open-closed fields, this expression reduces to V_{slow}, whereas, far from such a boundary, that is, deep within a coronal hole, it reduces to V_{fast}. For the DCHB model, then, the specification of the velocity profile depends only on the minimum distance of the field line foot-point to a coronal hole boundary.

2.3. The Wang-Sheeley-Arge Model

The WSA model has been successively refined since its initial development in the late 1990's at NOAA's Space Weather Prediction Center (SWPC) and was recently a key component in the first research model transitioned to space weather operations [*Farrell*, 2011]. It began life as a set of minor adjustments to the WS model, tuning the free parameters using more thorough comparisons with *in-situ* measurements. Then, the relationship was generalized, and a term based on the DCHB model was appended [*Arge et al.*, 2004]. The WSA prescription for solar wind speed at $30R_S$ is as follows :

$$V_{WSA}(f_s, d) = V_{slow} + \frac{(V_{fast} - V_{slow})}{(1+f_s)^{\alpha}} \left(\beta - \gamma e^{-(d/w)^{\delta}}\right) \quad (4)$$

The parameters v_{slow}, v_{fast}, d, w, and α are similar to those defined for the WS and DCHB models. In addition, the parameters β, γ, and δ have been introduced. Moreover, the entire right-most bracketed term is sometimes raised to a power, e.g., 7/2. According to Arge (Personal Communication, 2010), setting $v_{slow} = 240$km/s, $v_{fast} = 675$km/s, $\alpha = 1/4.5$, $\beta = 1$, $\gamma = 0.8$, $w = 2.8$, and $\delta = 3$ produce the best matches with GONG and SOLIS measurements. It should be noted, however, that some of these parameters are adjusted for different observatories. For Mount Wilson and Wilcox solar observatories, for example, they found a better match using: $v_{slow} = 250$km/s, $v_{fast} = 680$km/s, $\alpha = 1/3$, $w = 4$, and $\delta = 4$, with β and γ remaining the same. In the interests of tractability, in this study, we will assume $\beta = 1$ and $\gamma = 0.8$, varying the remaining 5 parameters. In summary, we note that, for the WSA model, the specification of the velocity profile depends both on the minimum distance of the field line foot-point to a coronal hole boundary (d) as well as the expansion factor (f_s). In the limit that $\gamma \to 0$, the WSA model approaches the WS model, and in the limit that $\alpha \to 0$, the WSA model approaches the DCHB model.

We should emphasize that we are exploring different empirical techniques and our prescription of the WSA model is not necessarily the same as that currently implemented at NOAA and/or NASA's CCMC. For example, the "official" WSA model incorporates a Schatten current sheet model [*Schatten*, 1971], which is omitted in our analysis. However, we have attempted to distill the most salient features of each method.

2.4. Relationship between Expansion Factor, Coronal Hole Boundaries, and the HCS

Although they are distinct constructs, the expansion factors of coronal magnetic field lines, the locations of coronal hole boundaries, and the position of the HCS are all complementary, but incomplete descriptions of the coronal magnetic field. In some sense, they are the more traditional structures that define the "magnetic skeleton" of the Sun's magnetic field. And, while newer concepts, such as quasi-separatrix layers, squashing factors, and spines [*Longcope*, 2005] would probably provide a more rigorous description of the underlying structure, since our focus here is on comparing techniques that rely on these more established quantities, we will limit our discussion to them.

Consider first the expansion factor of open magnetic field lines. This is estimated by the amount that the radial field has decreased from the photosphere to some reference height in the corona, beyond the $1/r^2$ divergence one would expect for a monopole field. Visually, it can be interpreted as the amount that a local bundle of open field lines expand as you follow them up through the corona. Deep within large polar coronal holes, this is a relatively low number, but closer to the boundary between open and closed field lines it increases as field lines have to fan out more to fill the space left by the closed field lines. Thus, at least intuitively, we would expect an inverse relationship between the distance from the coronal hole boundary and expansion factor. However, other coronal structures can modulate the value of the expansion factor, and these changes are not in any obvious way related to the DCHB. Pseudo-streamers, for example, are white-light structures in the corona built from double-loop systems [*Riley and Luhmann*, 2012]. While they are associated with coronal hole boundaries, and so, within the DCHB idea produce slow wind, they are also associated with anomalously small expansion factors, which, according to the WS prescription, would imply very high speeds [*Riley and Luhmann*, 2012; *Wang et al.*, 2007].

The HCS is the heliospheric extension of the solar neutral line, that is, it separates magnetic fields of one polarity from those of the opposite polarity. Coronal hole boundaries, which are defined at the solar surface, if traced up through the solar atmosphere, merge together, and form the HCS. Therefore, one might anticipate at least a superficial association between the DCHB and the location of the HCS. However, going from the photosphere to the origin of the HCS, one loses information about the structure of coronal holes themselves. Thus, the HCS is a "filtered" proxy for the location of coronal holes.

To illustrate the relationship between the location of coronal holes, the DCHB, expansion factor, and the location of the HCS, we have computed and displayed each for CRs 1913 and 2060 in Figures 1 and 2, respectively. CR 1913 and 2060 are well-studied intervals occurring at the cycle 22/23 minimum and just prior to the 23/24 minimum, respectively. These results were computed using solutions available online at www.predsci.com/mhdweb. The top panel in each case shows that, during these periods, there were well established polar coronal holes poleward of 60° in both hemispheres. The middle panel illustrates how the angular distance (in radians) from the boundary of the nearest coronal hole appears, when mapped out along field lines from the base of the corona to $30R_S$. The green line tracing through the minimum in the contours is the location of the HCS, that is, where $B_r = 0$. Finally, the bottom panel summarizes the areal expansion factor of magnetic field lines traced from $30R_S$ back to the surface of the Sun, plotted with reference to their location at $30R_S$. The expansion factor is most sensitive to the location of the HCS, with large expansion factors (i.e., low speeds) narrowly entrained about it.

Focusing first on CR 1913 (Figure 1), we note several points. First, the only longitudinal asymmetry in the coronal holes is due to an active region located near the equator at $\sim 270°$ longitude. This causes the two equatorial spurs in both polar coronal holes. Second, the DCHB, which is a tracer for the band of slow wind, encompasses the HCS. Thus, here, the two quantities are relatively well correlated with one another. It should be noted, however, that there is considerably more structure in the DCHB. Clearly, the DHCB produces a more complex velocity profile than could have been derived from a technique based on angular distance from the HCS. Third, the expansion factor (bottom panel) also traces the HCS closely, with largest values (corresponding to slow speed) aligned with it. Fourth, the DCHB increases much more gradually than the expansion factor decreases moving away from the HCS. Fifth, there are pockets of low expansion factor (deep purple) that branch off and return to the HCS (e.g., south of the equator, centered at 240° longitude. This would correspond to wind speeds greater than over the poles of the Sun.

Similar points can be made for CR 2060 (Figure 2). However, there are some important distinctions. First, several lower-latitude coronal holes, as well as polar coronal hole extensions were present. Consider the DCHB (and hence speed) profile at 240° longitude. While there is a clear minima associated with the HCS in the southern hemisphere, at $\sim -20°$ latitude, a second minimum can be found in the northern hemisphere, at $+15°$. This structure, it turns out is associated with a pseudo-streamer [*Riley and Luhmann*, 2012]. Second, the DCHB profile is even more complex, with spurs of low values (and hence low speeds) breaking away from the HCS and arcing back. Third, the apparent presence of equatorial coronal holes has broken the relatively close association between HCS, EF, and DCHB. As the bottom panel shows, EFs associated with the spurs in the middle panel are regions of low expansion factor and, hence, high speed. As noted earlier, the presence of the pseudo-streamers provides an ideal way to differentiate between the two models, with expansion factor predicting fast speed [*Wang et al.*, 2007] and DCHB predicting slow speed [*Riley and Luhmann*, 2012]

To illustrate these concepts more concretely, in Figures 3 and 4 we summarize the computed speeds at $30R_S$ for the WS, DCHB, and WSA models, together with the trace that an equatorially-located spacecraft would measure. (Time runs from the right to the left in this presentation). Considering the WS profile first (top panel): There is a band of slow flow wind tracing the location of the HCS, but pockets of extremely fast ($>$ 800 km/s) "hang" off it. In contrast, both the DCHB and WSA models show a much broader band of slow flow also organized about the HCS. The residual effects of the WS model's

$1/f_s^\alpha$ term can be seen in the WSA solution as very localized speed enhancements at $\sim 240°$ and $\sim 300°$ longitude.

2.5. Mapping Solar Wind Streams from $30R_S$ to 1 AU

Once $\mathbf{B}$ and $\mathbf{v}$ at $30R_S$ have been computed, they could be used as boundary conditions to drive a global heliospheric MHD model. However, for parametric sensitivity studies, such an approach is impractical: A single solution may take several hours to complete. Thus, even at modest resolutions, it would be infeasible to compute hundreds or thousands of solutions. As a pragmatic compromise, we developed a simple numerical algorithm for mapping solar wind streams from near the Sun to 1 AU or elsewhere in the solar system [*Riley et al.*, 2011]. It neglects magnetic and thermal pressure terms and is restricted to 1-D; however, it is robust and performs reasonably well. In particular, we found that this technique, when coupled with an acceleration model to account for the residual acceleration of the solar wind that occurs beyond $30R_S$, produced mappings at 1 AU that were substantially the same (CC = 0.98) as full three-dimensional heliospheric MHD solutions [*Riley et al.*, 2011].

3. Model Comparisons with *in-situ* Measurements

In this section, we describe comparisons for one specific interval in detail; CR 2060 (August 2007). Next, we compute and interpret model predictions for a selection of 14 Carrington rotations spanning from CR 1913 to 2083. Finally, we summarize a statistical study of model comparisons spanning the entire last solar cycle, from CR 1900 to 2080.

CR 2060 occurred toward the end of solar cycle 23 and was devoid of large-scale transient activity. Moreover, the ACE spacecraft was situated serendipitously at a location from which it could sample both helmet and pseudo-streamer structure during the same rotation [*Riley and Luhmann*, 2012]. For each model solution for this interval, we used data from the MDI magnetograph onboard the SOHO spacecraft to compute either PFSS or MHD coronal solutions. Next, we: (1) computed velocity maps of the speed at $30R_S$; (2) mapped out the solution to 1 AU as described in Section 2.5; and (3) compared with *in-situ* measurements by ACE/Wind spacecraft.

For the case study, we defined hypercubes in the appropriate parameter space. For the WS model, the cube consisted of V_{slow}, V_{fast}, and $\Delta\phi$ ($10 \times 10 \times 10$); the last parameter being included in the analysis to account primarily for any phase mismatch caused by the fact that the wind has an acceleration profile from the solar surface to $30R_S$, which is not accounted for in these simple models. For the DCHB model, we considered a 5-D hypercube ($6 \times 6 \times 6 \times 6 \times 10$) consisting of the four intrinsic model parameters plus $\Delta\phi$ and a 6-D hypercube ($6 \times 6 \times 6 \times 6 \times 6 \times 10$) for the WSA model. Table 1 summarizes the hyper-volume of parameter space for each of the three models. These ranges were based on a series of preliminary calculations aimed at constraining the multi-dimensional parameter space.

Rather than using a technique such as steepest descent to trace our way to the minimum (optimum solution) in this parameter space, because the algorithm was relatively quick, we constructed solutions for every point in the hypercube, retaining only those that optimized the PCC as well as the root mean square error (RMSE) with observations at 1 AU. The PCC is a measure of the linear correlation between two variables, where total positive/negative correlation is given by +1/-1 and no correlation is given by zero. The RMSE, on the other hand, is a measure of the standard deviation of the differences between predicted and observed values. This allowed us to explore the global properties of minima within the parameter space, while still providing approximate estimates for the optimal parameters. For simplicity, we base our analysis exclusively on PCC-optimized solutions. The distinctions between PCC, RMSE, and other viable metrics will be reported elsewhere.

3.1. Case Study: CR 2060

In Figures 5, 6, and 7, we summarize examples of WS, DCHB, and WSA solutions that produced the best correlations. We do not claim that, even for this rotation, these are the optimum parameters; However, we do believe that they are representative of the hypercube's global minimum.

Figure 5 presents a comparison of the WS model with observations for CR 2060. Panel (a) shows the radial speed as a function of longitude and latitude. Several points are worth noting. First, the speed at mid and high latitudes is only modestly above 400 km/s. This disagrees with Ulysses observations [*McComas et al.*, 2006], which suggest that, at least during the declining phase and at solar minimum, the speed of the high-latitude wind is $\sim$ 760 km/s. Second, the highest speeds are located at, and around the heliographic equator. Third, the slowest speeds undulate about the heliographic equator (dark blue trace) following the location of the HCS. From Equation (1), we can understand this distribution: Where the expansion factors are largest, around the HCS, the speeds are slowest. More modest expansion factors produce the medium-speed wind populating much of the map, and small pockets of low expansion factor produce the highest speed winds (red bands).

To compare this trace with *in-situ* measurements we could: (1) map the model results out to 1 AU (as described in Section 2.5) and compare directly with observations; or (2) map the 1 AU observations back to $30R_S$ and compare directly with model results. Both approaches introduce errors; however, both offer complementary and distinct information. Focusing first on the comparison at $30R_S$, Figure 5(b) compares the velocity profiles at $30R_S$, a location sufficiently close to the Sun that dynamical effects, such as stream compression, should not have begun. Of course, the ballistically-mapped-back data cannot be purged of this evolution, which is the primary limitation of such a comparison. Nevertheless, we infer that the WS model has captured perhaps two of the high-speed streams, but fails to predict slow solar wind at both the start and end of the rotation. Interestingly, it predicts localized "beams" of high-speed wind as the spacecraft intercepts regions of low expansion factor.

The comparison at 1 AU (Figure 5(c)) emphasizes the dynamic evolution of the streams. The localized high-speed streams have merged into generally fast solar wind. However, the main discrepancy is still present: The observations include slow wind during the second half of the rotation, whereas the WS model predicts fast wind. For this rotation, the best PCC that could be achieved was -0.061, with $V_{slow} = 500$ km/s and $V_{fast} = 1000$ km/s (Table 2).

Figure 6 makes a similar comparison using the DCHB model. The speed map in the top panel shows fast wind at high latitudes and a band of structured slow flow about the equator, matching the pattern in Figure 4(b). The overall speeds are somewhat lower than 1 AU measurements because there is an outward acceleration of wind beyond $30R_S$. Figure 6 (b) compares the ballistically-mapped back speed with the model results at $30R_S$.

From this, we infer an approximate agreement at the largest scales, with some notable discrepancies, particularly between $85° - 160°$ longitude. At 1 AU (Figure 6 (c)), the profile matches reasonably well. Of particular note is that the model predicts slow solar wind from 210° through the remainder of the rotation, in agreement with observations.

Finally, in Figure 7, we show the same comparison using results from the WSA model. Focusing on the distinguishing features between this and Figures 5 and 6, we note the small "islands" of fast wind attached to the band of slow flow in the WSA solution. There is a particularly long "wisp" of fast wind in the southern hemisphere between 110° and 190°. However, since the spacecraft's trajectory remained in the northern hemisphere, it would not have intercepted this structure. In summary, the spacecraft profiles are substantially similar to those of the DCHB model (Figure 6), and the degree of correlation (PCC = 0.672) is roughly the same for this rotation (Table 2).

3.2. Model Parameter Estimates for a Selection of Campaign Rotations

We extended our analysis to a selection of 14 Carrington rotations spanning from the 22/23 minimum to the 23/24 minimum, by computing hyper-matrices of solutions, varying the input parameters for each of the three models. The parameter space explored for each model is summarized in Table 1, which represent broad, but reasonable ranges for each of these parameters. The solutions producing the highest PCC for each rotation and model are summarized in Table 2. These rotations were not chosen because they resulted in high values of PCC, but were approximately equally spaced between 1913 and 2083. In some cases, poor or even unavailable synoptic maps necessitated a shift to an adjacent rotation. Considering first the value of PCC, we note: (1) a strong variation from essentially no correlation ($PCC \sim 0$) to high correlation ($PCC > 0.8$); and (2) the highest correlations occur at the beginning and end of the interval, i.e., at near-solar minimum conditions. The values of the parameters are most tightly clustered for the DCHB model, followed by the WSA, then WS model.

3.3. Parametric Study Spanning more than Three Solar Cycles

To estimate the robustness of the parameters we derived for the parametric studies in Section 3.2, we conducted sensitivity studies for 200 rotations spanning Carrington rotations 1900 through 2100 (September, 1995 through August, 2010). This corresponds to more than one solar cycle and required data from both Kitt Peak's Vacuum Telescope (KPVT) and SOLIS, the switch occurring at CR 2007. We chose representative parameters based on the results in Table 2, combining the best repeated values for the rotations with the highest PCC values. We repeated the exercise with other reasonable choices to verify that, at least statistically, the results were not sensitive to which choice was made. We reiterate, the model parameters chosen are not necessarily the optimum ones; it is quite possible that they will depend on the magnetogram used to compute the solution, the precise details of the model implemented, and may even have solar cycle dependencies. We also confirmed that they were in reasonable agreement with the values in the original papers outlining that particular method.

Historically, the WS, WSA, and DCHB models were developed and refined using different global models. In particular, the WS and WSA models were validated against in-situ measurements using PFSS models, while the DCHB model relied on MHD solutions. To address this, we computed solutions using results from both the PFSS and MHD models.

In Figure 8 we present the computed PCCs for the WS, DCHB, and WSA models for Carrington rotations 1900 through 2100 based on PFSS model solutions. If no magnetogram data were available, that CR was omitted. Of the 200 possible solutions, 174 were retained for analysis. Our PFSS model is virtually the same as that used by other researchers [e.g. *Wang and Sheeley*, 1990; *Arge and Pizzo*, 2000],with the notable difference that numerically, we rely on a finite difference scheme, rather than the spherical harmonic approach [*Altschuler and Newkirk*, 1969], which, in principle, allows us to generate solutions at much higher spatial resolution. The top panel summarizes the correlation coefficient for each rotation while the middle panel shows an 11-rotation running average, thus, emphasizing longer-term variability. The three histograms at the bottom show the distribution of correlation coefficients.

Focusing first on panel (a), we note that the three techniques generally track one another quite well, with the WS model systematically slightly lower, and particularly during the interval from $\sim$ 2007 through $\sim$ 2009 (Figure 8, middle panel). This coincided with the appearance of pseudo-streamers, which, as we have noted, represents conditions under which the WS model is not likely to perform well [*Riley and Luhmann*, 2012]. We note further that there is considerable variability from one rotation to the next.

The bottom panels of Figure 8 show how the PCCs are distributed: all three approaches generally show positive correlations. The median (mean) value of the WS PCC is 0.27 (0.25), while the median (mean) values of the DCBH and WSA coefficients are 0.35 (0.34) and 0.39 (0.35), respectively. Moreover, only 25% of the CRs produced PCCs exceeding 0.5 using the WS method, whereas 35% and 36% of the same CRs produced correlations that exceeded 0.5 using the DCHB and WSA techniques.

In Figure 9 we show the equivalent plots based on the MHD solutions. Considering the time series in the top panel, we note: (1) again, there is considerable variability from one rotation to the next; (2) the PCC generally drops from 1996 through 2000-2002, then rises and stays higher from 2004 through 2010; (3) the WS coefficient is systematically lower than either the DCHB or the WSA coefficient; (4) the WS coefficient is notably lower between CR 2060 through 2080; and (5) there are a few CRs where the WS coefficient is significantly better than either the DCHB or WSA coefficients.

Panel (b) of Figure 9 shows that , on average, the WS model shows relatively poor correlation throughout the entire interval, with a period around 2003-2004 that shows the highest correlation. Both the DCHB and WSA models show larger average PCCs, with the highest sustained correlations in the latter half of the period (2004-2010).

The most striking difference between the MHD results and those summarized in Figure 8 lies in how the distribution of WS model results has changed. Using the MHD solutions, the average WS correlations were only slightly above zero. In contrast, when the PFSS solutions are used to compute the WS model speeds, the resulting distribution (lower-left, green histogram) is significantly more skewed to positive values, and is, at least qualitatively, comparable to the DCHB and WSA results.

For the MHD solutions, the median (mean) value of the WS PCC is 0.06 (0.07), while the median (mean) values of the DCBH and WSA coefficients are 0.40 (0.35) and 0.36 (0.33), respectively. Moreover, only 7% of the 174 CRs produced PCCs exceeding 0.5 using the WS method, whereas 40% and 34% of the same CRs produced correlations that exceeded 0.5 using the DCHB and WSA techniques.

Unlike the WS model, the DCHB and WSA models do not seem to depend significantly on whether the input magnetic field is computed from and MHD or PFSS model. It could be argued that the MHD solutions provide slightly higher correlations on average;

however, this could also be the result of parameters that were not optimally tuned for the PFSS field model.

4. Summary and Discussion

In this study, we have compared three different techniques for determining the profile of the bulk solar wind flow speed based on the structure of the coronal magnetic field. We found that the DCHB and WSA models performed substantially better than the WS model when an MHD solution was used as input. In contrast, when a PFSS solution was used, the WS technique improved significantly.

Our analysis showed that, regardless of whether an MHD or PFSS solution was employed, the WS model was systematically worse than either the WSA or DCHB model from mid-2007 through mid-2009 (Figures 9 and 8). Although there may be other possible explanations for this, we believe that the most compelling is that during this interval, pseudo-streamers were frequently present. As we have shown here and elsewhere [*Riley and Luhmann*, 2012], the WS model appears to fail in the vicinity of pseudo-streamers, where it predicts extremely fast wind, in contrast to the DCHB model, which, in agreement with observations, predicts slower wind.

This study demonstrates that the DCHB and WSA models produce results that are remarkably similar. It is worth understanding why this is so. From the expression for V_{wsa} (Equation (4)), we note that the WS contribution to the speed is of the form: $1/(1 + f_s)^{\alpha}$, where $\alpha \sim 0.3 - 0.4$ (Table 2). Assuming $\alpha = 0.3$, as suggested by Arge (Personal Communication, 2014), with the expansion factor ranging from $6.5 \rightarrow 40$ for CR 2060, we estimate that this factor varies from 0.33 to 0.55 across the reference sphere. On the other hand, the DCHB-like term is of the form $(1 - 0.8e^{(-(d/4)^4)})$. Again, the MHD solution indicates that d varies from $0 \rightarrow 23^\circ$. Thus, the DCHB term varies from $0.2 \rightarrow 1$, and, therefore, modulates the speeds far more than the WS term in the WSA formula. To a large degree then, the WSA formula for computing solar wind speed is governed by the distance from the nearest coronal hole boundary, and not the flux tube expansion factor term. In fact, we suspect that the slightly lower PCC values from the WSA model, as compared with the DCHB model during the 2007-2009 interval (Figures 8 and 9) may be due to the presence of the WS-like term. Ironically, the presence of an expansion factor term in the prediction of the solar wind speed is lowering its predictive power.

There is a significant difference in the quality of the WS solutions computed using the MHD and PFSS magnetic fields. On the other hand, the DCHB and WSA model results are less sensitive to the input field configuration. We believe that the PFSS model, which requires that the field becomes radial at some specific height, say $2.5R_S$, is introducing additionally variability into the expansion of the coronal fields lines, which is not present in the MHD solution, but which improves the accuracy of the WS approach.

Our study involved a number of assumptions and sources of errors that could potentially have affected our results and their interpretation. The photospheric magnetic fields used to drive the coronal solutions, for example, are not precisely known [e.g. *Riley et al.*, 2012a], which will impact a model's ability to predict solar wind speed at 1 AU. Moreover, the models are limited and contain assumptions that, in some cases, cannot be rigorously defended, such as quasi-stationarity (either on sub-rotation timescales or solar cycle), or the lack of any turbulence or waves in the model solutions. However, it is precisely these limitations that the study has attempted to estimate, and which are incorporated into the computed PCCs.

Our incorporation of the parameter ϕ to account for shifts in longitude between the model results and observations, while often improving the fit, suggests another source of error that cannot be easily accounted for. As shown in Table 2, values between -14° and $+14^\circ$ were often found. These represented the maximum allowable values for ϕ. However, we could not justify using values larger than this based on any known physical phenomena (e.g., acceleration of the solar wind from, say, $1R_S$ to $30R_S$). The values computed for ϕ spanned this entire range, with no obvious systematic bias. In future studies, we will attempt to understand the variability of ϕ and its relationship with other model parameters, including input magnetograms, model type, and phase of the solar cycle.

Here, we relied on estimates of the PCC to assess the quality of the model solutions. We also computed RMSE, and while there were some discrepancies between which solution was optimal, for the purposes of this study, they were not material. In addition to PCC and RMSE, there are a number of other metrics that could be considered [e.g. *Owens et al.*, 2008a]. In future studies, we plan to incorporate other types of skill scores, such as the arrival time of sector boundary crossings into the analysis.

Ultimately, the ideal approach would be a systematic parametric study adjusting all possible inputs, models, and parameters iteratively, using a multidimensional conjugate gradient type technique, such as the steepest descent method. However, in practice, given the time it takes to compute a single coronal solution, map speed profiles along field lines, and compute heliospheric solutions, it would not be feasible to do this iteratively. The analysis described here, of using a single set of synoptic maps, a limited set of semi-empirical models, and a course hyper-grid of model parameters is a first-step toward this goal. In future studies, we plan to investigate refinements to this analysis. For example, are there systematic solar-cycle dependencies in the model parameters [e.g. *Lee et al.*, 2011]? Do some synoptic magnetograms (e.g., for a particular observatory or prepared in a particular way) give consistently better matches? Are there any conditions under which the WS model outperforms the DCHB or WSA models?

Should these results withstand further scrutiny, they suggest that the perpendicular distance from the coronal hole boundary is the primary structural feature about which the solar wind flow speed is organized. We may further theorize that such a result more naturally favors a "boundary layer" explanation for the origin of the slow solar wind, such as "interchange reconnection" or a Rayleigh-Taylor instability [*Suess et al.*, 2009], since this component would naturally originate at the boundary between open and closed field lines. On the other hand, the "expansion factor" theory, by definition, requires the slow solar wind to be organized around variations in the flux tube expansion factor.

Our study, however, does not conclusively show that expansion factor plays no role. Instead, we have suggested that its association with the boundary between open and closed field lines is responsible for the observed correlation. On the other hand, it is possible that expansion factor is playing a minor role in the modulation of solar wind speed, perhaps in the fast solar wind and near coronal hole boundaries. Additionally, we have computed expansion factor at a particular reference height ($2.5R_S$). It may be that the detailed changes in expansion factor along a flux tube are also important, as has been suggested by *Wang et al.* [2012] in relation to pseudo-streamers. Finally, it is worth noting that there is tentative evidence that expansion factor may modulate the speed of fast solar wind, relatively deep within coronal holes. For example, in a study by *McGregor* *et al.* [2011], the WSA model produced small-scale modulations within large-scale polar coronal holes, which appear to match Ulysses observations as it traversed the solar poles in late 1994 through early 1995. Are these driven by the expansion factor term? Further investigation of these open questions may form fruitful lines of research.

In closing, we reiterate the two main points of this study. First, the WSA model is driven primarily (although not exclusively) by the distance from the coronal hole boundary. And second, the DCHB and WSA models typically perform better than the original WS model, which is based solely on the expansion factor of magnetic field lines, particularly when pseudo-streamers are present.

Acknowledgments. The authors gratefully acknowledge the support of NASA (Causes and Consequences of the Minimum of Solar Cycle 24 program, LWS Strategic Capabilities program, Heliophysics Theory Program, and the STEREO IMPACT team) and NSF (Center for Integrated Space Weather Modeling (CISM) program). The data used in this study are all publicly available. MDI synoptic maps are available from Stanford University (http://soi.stanford.edu), KPVT and SOLIS maps are available from the National Solar Observatory (http://www.nso.edu), and *in situ* measurements at 1 AU can be retrieved from NASA's COHOWeb (http://omniweb.gsfc.nasa.gov/coho/). Finally, the authors would like to express their gratitude to the reviewers for their thoughtful comments.

References

Altschuler, M. D., and G. Newkirk, Magnetic Fields and the Structure of the Solar Corona. I: Methods of Calculating Coronal Fields, *Solar Phys.*, *9*, 131–+, 1969.

Antiochos, S. K., Z. Mikić, V. S. Titov, R. Lionello, and J. A. Linker, A model for the sources of the slow solar wind, *Astrophys. J.*, *731*, 112, doi:10.1088/0004-637X/731/2/112, 2011.

Arge, C. N., and V. J. Pizzo, Improvement in the prediction of solar wind conditions using near-real time solar magnetic field updates, *J. Geophys. Res.*, *105*, 10,465, doi:10.1029/1999JA900262, 2000.

Arge, C. N., D. Odstrcil, V. J. Pizzo, and L. R. Mayer, Improved Method for Specifying Solar Wind Speed Near the Sun, in *Solar Wind Ten*, *AIP Conf. Proc.*, vol. 679, edited by M. Velli, R. Bruno, F. Malara, and B. Bucci, p. 190, doi:10.1063/1.1618574, 2003.

Arge, N., J. G. Luhmann, C. J. Odstrcil, C. J. Schrijver, and Y. Li, Stream structure and coronal sources of the solar wind during the May 12th, 1997 CME, *J. Atmos. Sol.-Terr. Phys.*, *66*, 1295–1309, 2004.

Bussy-Virat, C., and A. Ridley, Predictions of the solar wind speed by the probability distribution function model, *Space Weather*, 2014.

Cranmer, S. R., An efficient approximation of the coronal heating rate for use in global sun-heliosphere simulations, *Astrophys. J.*, *710*, 676, doi:10.1088/0004-637X/710/1/676, 2010.

Farrell, P., New Space Weather Forecasting Model Going Operational with National Weather Service, *www.bu.edu/cas/news/press-releases/cism/*, 2011.

Fisk, L., Motion of the footpoints of heliospheric magnetic field lines at the sun: Implications for recurrent energetic particle events at high heliographic latitudes, *J. Geophys. Res.*, *101*, 15,547, doi:10.1029/96JA01005, 1996.

Hakamada, K., and S. Akasofu, A cause of solar wind speed variations observed at 1 A.U., *J. Geophys. Res.*, *86*, 1290, doi:10.1029/JA086iA03p01290, 1981.

Jian, L. K., C. T. Russell, J. G. Luhmann, P. J. MacNeice, D. Odstrcil, P. Riley, J. A. Linker, R. M. Skoug, and J. T. Steinberg, Comparison of Observations at ACE and Ulysses with Enlil Model Results: Stream Interaction Regions During Carrington Rotations 2016 - 2018, *Solar Phys.*, *273*, 179–203, doi:10.1007/s11207-011-9858-7, 2011.

Laming, J. M., On collisionless electron-ion temperature equilibration in the fast solar wind, *Astrophys. J.*, *604*, 874, doi:10.1086/382066, 2004.

Lee, C., J. Luhmann, J. Hoeksema, X. Sun, C. Arge, and I. de Pater, Coronal field opens at lower height during the solar cycles 22 and 23 minimum periods: Imf comparison suggests the source surface should be lowered, *Solar Physics*, *269*(2), 367–388, 2011.

Longcope, D. W., Topological methods for the analysis of solar magnetic fields, *Living Reviews in Solar Physics*, *2*(7), 2005.

McComas, D. J., H. A. Elliott, J. T. Gosling, and R. M. Skoug, Ulysses observations of very different heliospheric structure during the declining phase of solar activity cycle 23, *Geophys. Res. Lett*, *33*, 9102–+, doi:10.1029/2006GL025915, 2006.

McGregor, S. L., W. J. Hughes, C. N. Arge, M. J. Owens, and D. Odstrcil, The distribution of solar wind speeds during solar minimum: Calibration for numerical solar wind modeling constraints on the source of the slow solar wind, *Journal of Geophysical Research (Space Physics)*, *116*, A03101, doi:10.1029/2010JA015881, 2011.

Norquist, D. C., and W. C. Meeks, A comparative verification of forecasts from two operational solar wind models, *Space Weather*, *8*(12), 2010.

Owens, M. J., N. U. Crooker, N. A. Schwadron, T. S. Horbury, S. Yashiro, H. Xie, O. C. St. Cyr, and N. Gopalswamy, Conservation of open solar magnetic flux and the floor in the heliospheric magnetic field, *Geophys. Res. Lett.*, *35*, 20,108–+, doi: 10.1029/2008GL035813, 2008a.

Owens, M. J., H. E. Spence, S. McGregor, W. J. Hughes, J. M. Quinn, C. N. Arge, P. Riley, J. Linker, and D. Odstrcil, Metrics for solar wind prediction models: Comparison of empirical, hybrid, and physics-based schemes with 8 years of L1 observations, *Space Weather*, *6*, 8001–+, doi:10.1029/2007SW000380, 2008b.

Owens, M. J., R. Challen, J. Methven, E. Henley, and D. R. Jackson, A 27 day persistence model of near-earth solar wind conditions: A long lead-time forecast and a benchmark for dynamical models, *Space Weather*, *11*(5), 225–236, 2013.

Pizzo, V., G. Millward, A. Parsons, D. Biesecker, S. Hill, and D. Odstrcil, Wang-Sheeley-Arge-Enlil Cone Model Transitions to Operations, *Space Weather*, *9*, 03004, doi:10.1029/2011SW000663, 2011.

Riley, P., and J. G. Luhmann, Interplanetary Signatures of Unipolar Streamers and the Origin of the Slow Solar Wind, *Solar Phys.*, *277*, 355–373, doi:10.1007/s11207-011-9909-0, 2012.

Riley, P., J. A. Linker, and Z. Mikić, An empirically-driven global mhd model of the corona and inner heliosphere, *J. Geophys. Res.*, *106*, 15,889, doi:10.1029/2000JA000121, 2001.

Riley, P., J. A. Linker, Z. Mikić, R. Lionello, S. A. Ledvina, and J. G. Luhmann, A comparison between global solar magnetohydrodynamic and potential field source surface model results, *Astrophys. J.*, *653*, 1510, doi:10.1086/508565, 2006.

Riley, P., R. Lionello, J. A. Linker, Z. Mikic, J. Luhmann, and J. Wijaya, Global MHD modeling of the solar corona and inner heliosphere for the whole heliosphere interval, *Solar Phys.*, p. 145, doi:10.1007/s11207-010-9698-x, 2011.

Riley, P., J. A. Linker, R. Lionello, and Z. Mikic, Corotating interaction regions during the recent solar minimum: The power and limitations of global MHD modeling, *J. Atmos. Solar-Terr. Phys.*, *83*, 1–10, doi:10.1016/j.jastp.2011.12.013, 2012a.

Riley, P., R. Lionello, J. A. Linker, Z. Mikic, J. Luhmann, and J. Wijaya, Global MHD modeling of the solar corona and inner heliosphere for the whole heliosphere interval, *Solar Phys.*, *274*, 361–3775, doi:10.1007/s11207-010-9698-x, 2012b.

Riley, P., et al., Relationship between ulysses plasma observations and solar observations during the whole sun month campaign, *J. Geophys. Res.*, *104*(A5), 9871, 1999.

Schatten, K. H., Current Sheet Model for the Solar Corona, *Cosmic Electrodynamics*, *2*, 232–245, 1971.

Shiota, D., R. Kataoka, Y. Miyoshi, T. Hara, C. Tao, K. Masunaga, Y. Futaana, and N. Terada, Inner heliosphere mhd modeling system applicable to space weather forecasting for the other planets, *Space Weather*, *12*(4), 187–204, 2014.

Suess, S. T., Y.-K. Ko, R. von Steiger, and R. L. Moore, Quiescent current sheets in the solar wind and origins of slow wind, *J. Geophys. Res.*, *114*, A04,103, doi:10.1029/2008JA013704, 2009.

Wang, Y., Y. Ko, and R. Grappin, Slow solar wind from open regions with strong low-coronal heating, *Astrophys. J.*, *691*, 760, doi:10.1088/0004-637X/691/1/760, 2009.

Wang, Y. M., and N. R. Sheeley, Solar wind speed and coronal flux-tube expansion, *Astrophys. J.*, *355*, 726, doi:10.1086/168805, 1990.

Wang, Y. M., and N. R. Sheeley, The high-latitude solar wind near sunspot maximum, *Geophys. Res. Lett.*, *24*, 3141, doi:10.1029/97GL53305, 1997.

Wang, Y. M., S. H. Hawley, and N. R. Sheeley, The magnetic nature of coronal holes, *Science*, *271*, 464, doi:10.1126/science.271.5248.464, 1996.

Wang, Y.-M., N. R. Sheeley, and N. B. Rich, Coronal pseudostreamers, *Astrophys. J.*, *658*, 1340, doi:10.1086/511416, 2007.

Wang, Y.-M., R. Grappin, E. Robbrecht, and N. R. Sheeley, Jr., On the Nature of the Solar Wind from Coronal Pseudostreamers, *Ap. J.*, *749*, 182, doi:10.1088/0004-637X/749/2/182, 2012.

Table 1. Size of hypercube used to identify optimum solutions

Model	V_{slow}	V_{fast}	α	ϵ	w	δ	ϕ
WS	$200 \rightarrow 500$	$500 \rightarrow 1000$	$1.0 \rightarrow 1.0$				$-14^{\circ} \rightarrow +14^{\circ}$
DCHB	$200 \rightarrow 400$	$400 \rightarrow 600$		$0.02 \rightarrow 0.06$	$0.015 \rightarrow 0.035$		$-14^{\circ} \rightarrow +14^{\circ}$
WSA	$200 \rightarrow 400$	$550 \rightarrow 750$	$0.3 \rightarrow 0.5$		$0.1 \rightarrow 0.4$	$3 \rightarrow 5$	$-14^{\circ} \rightarrow +14^{\circ}$

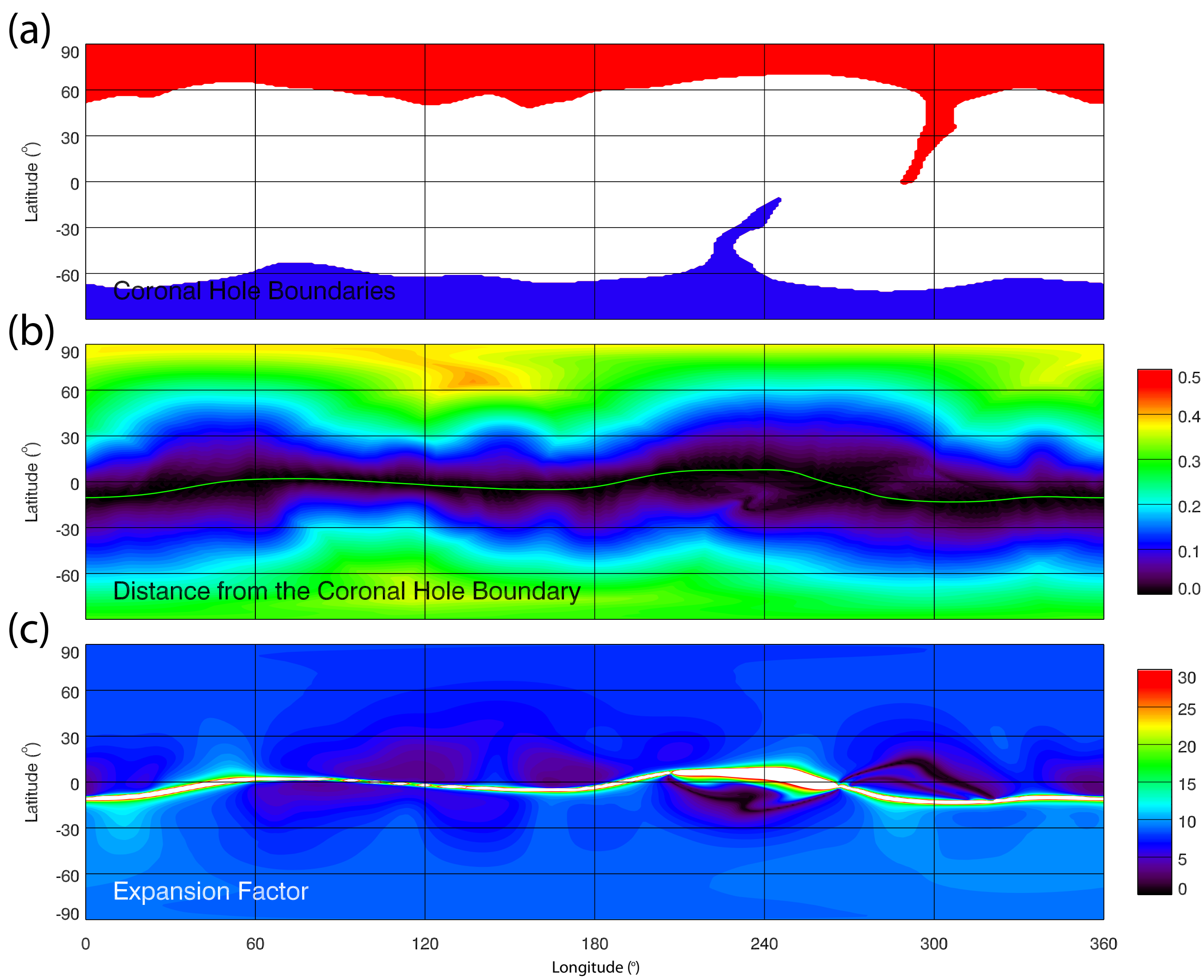

Figure 1. (Top) Coronal hole boundaries (at $1R_S$) as a function of heliographic longitude and latitude at the solar surface ($1R_S$) for Carrington rotation 1913. (Middle) Perpendicular distance from the nearest coronal hole boundary (in radians) at $30R_S$. The green line indicates the location of the HCS. (Bottom) the areal expansion factor of field lines, traced from $30R_S$ back to the solar surface but shown at $30R_S$. Values of expansion factor>30 are saturated and shown by the white band.

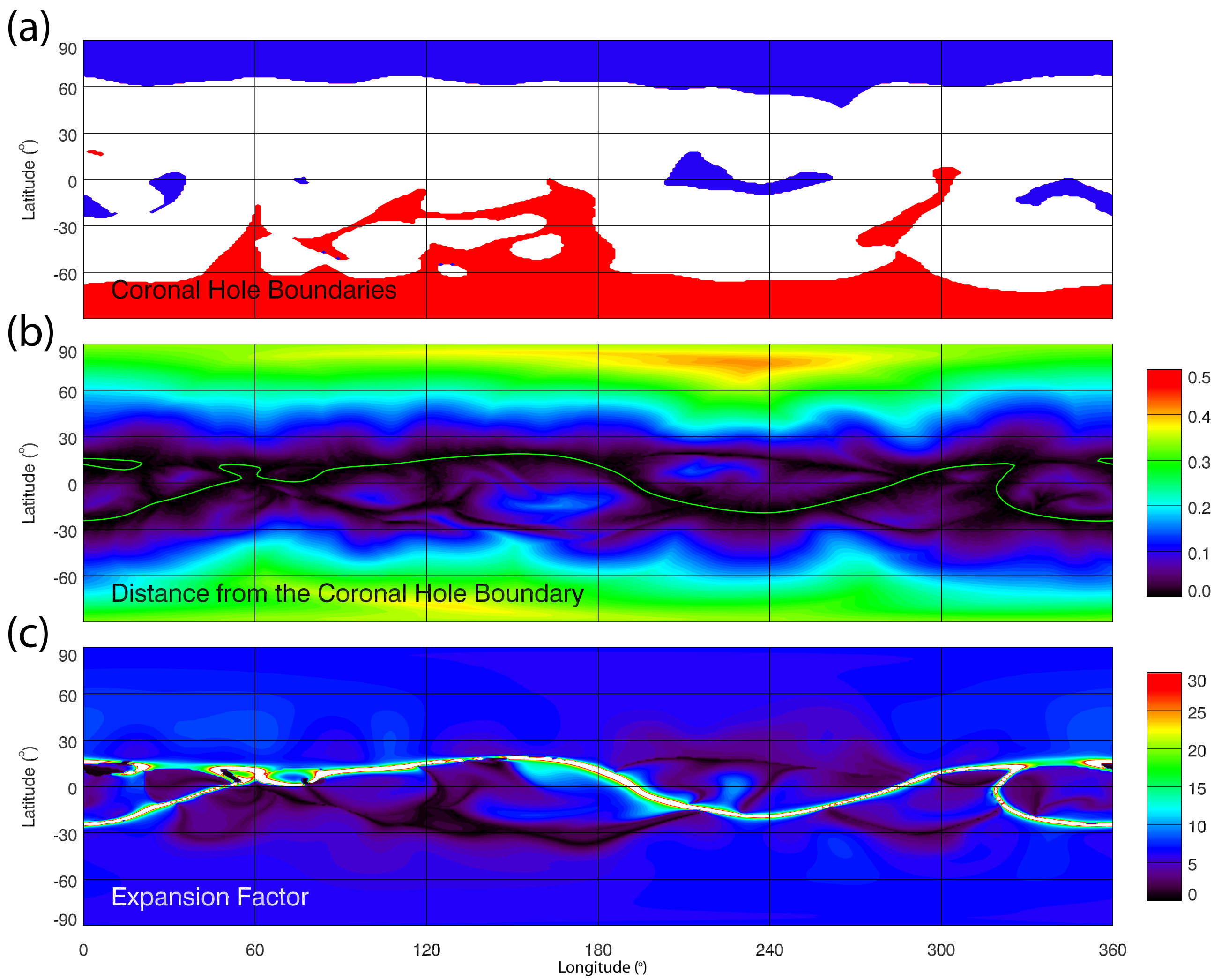

Figure 2. As Figure 1 but for CR 2060.

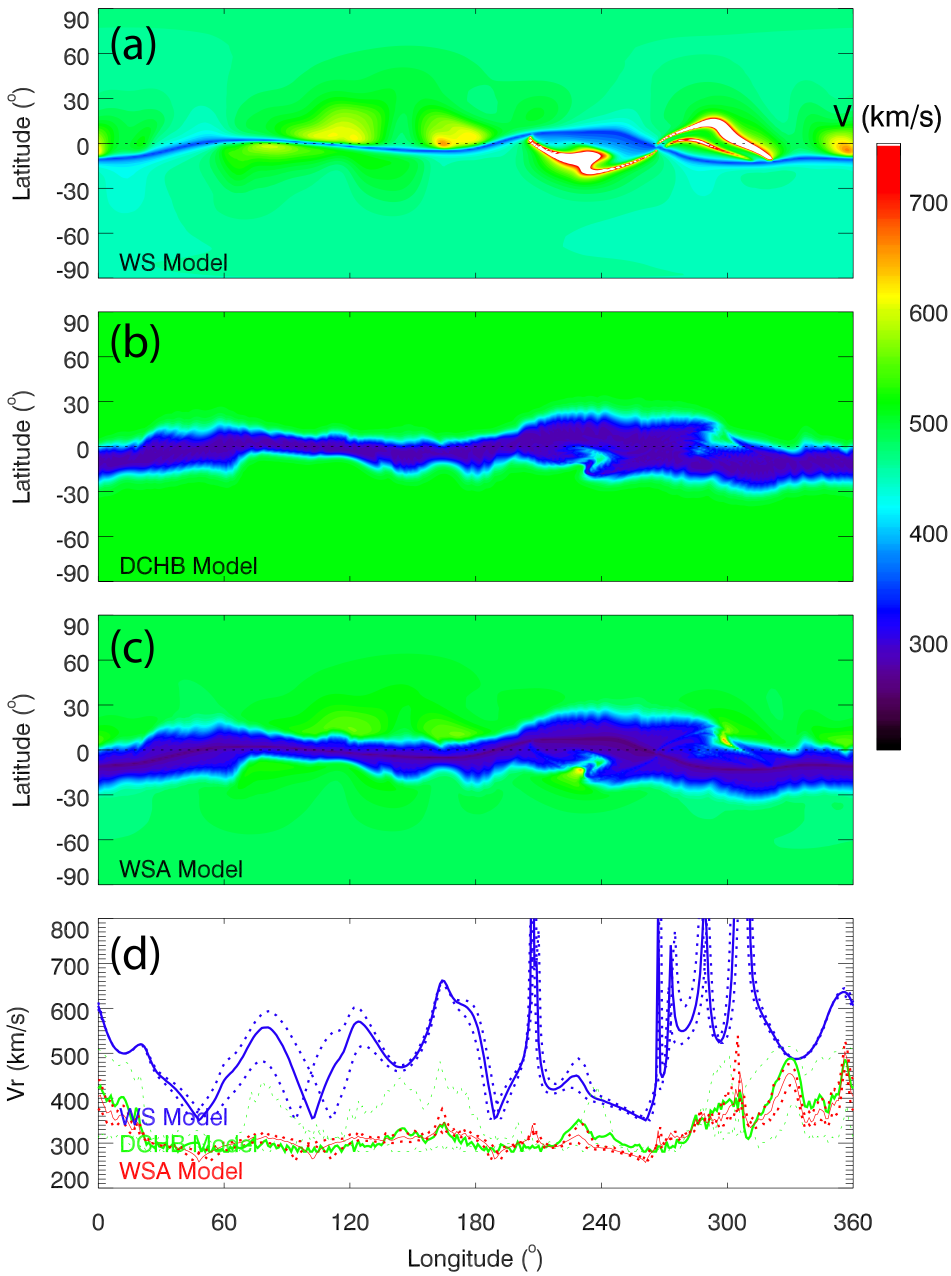

Figure 3. (a) Computed solar wind speed at $30R_S$ using the WS model as a function of longitude (x-axis) and latitude (y-axis) for CR 1913; (b) Computed solar wind speed at $30R_S$ using the DCHB model; (c) Computed solar wind speed at $30R_S$ using the WSA model; and (d) Comparison of the three model speeds at the equator as a function of Carrington longitude. The dashed curves give the computed solar wind speed $\sim \pm 1.25°$ latitude above and below the spacecraft.

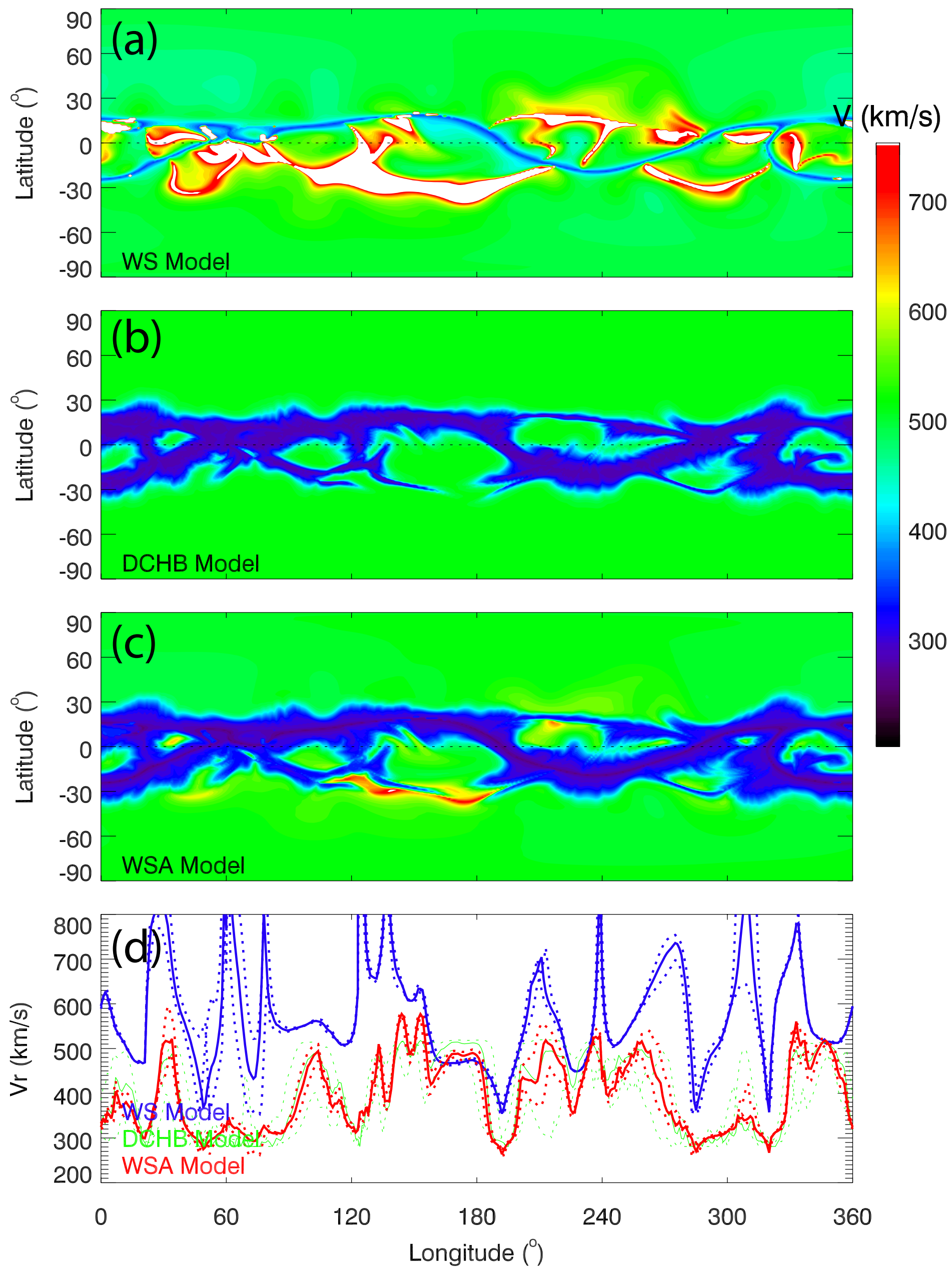

Figure 4. As Figure 3 but for Carrington rotation 2060.

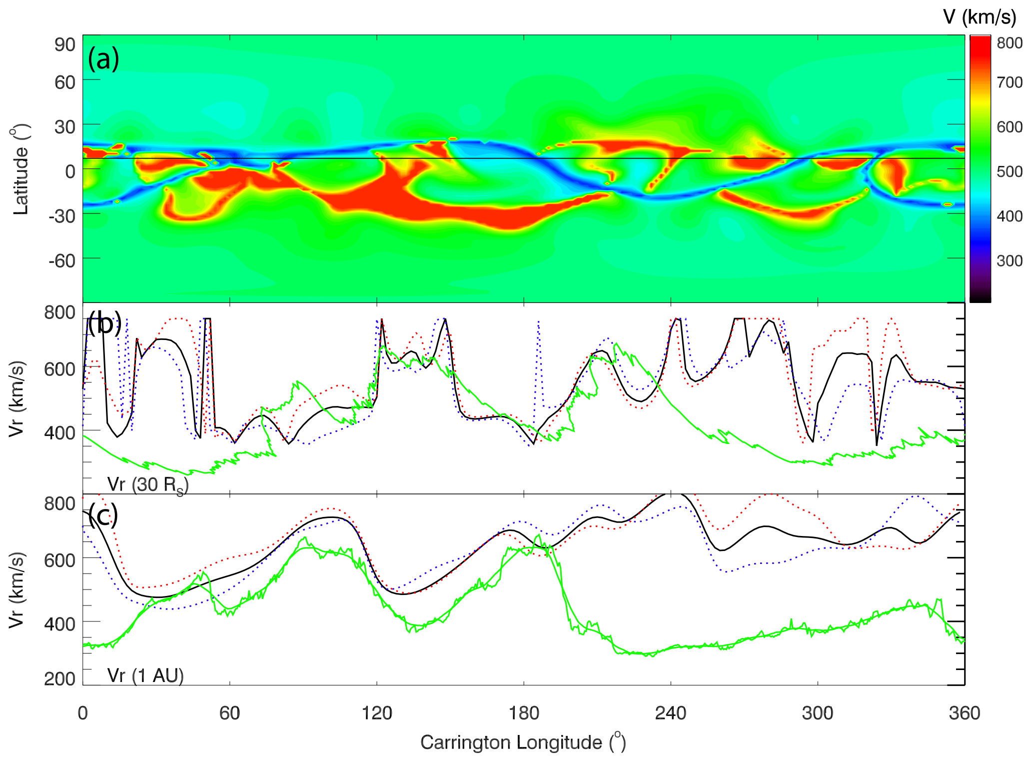

Figure 5. (a) Speed map as a function of longitude (x) and latitude (y) at $30R_S$ for the Wang-Sheeley (WS) model for CR 2060. The solid straight line marks the trajectory of the spacecraft, with time increasing from right to left. (b) Comparison of computed speed (black) at $30R_S$ and ballistically-mapped *in-situ* measurements of speed (green) at Earth mapped to $30R_S$. (c) Comparison of computed (black) and observed (green) solar wind speed at Earth. The dotted red and blue lines show profiles at $\pm 2°$ of the location of the spacecraft. The smooth green line is a 1-day running mean of the 1-hour in-situ measurements.

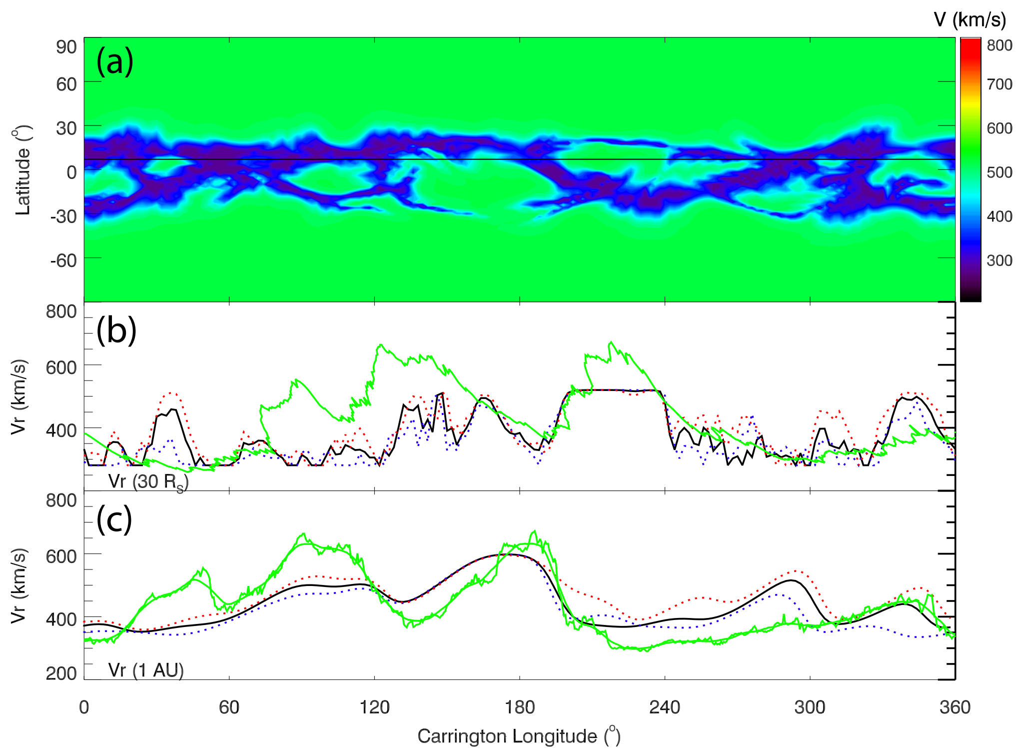

Figure 6. As Figure 5 but using the DCHB model.

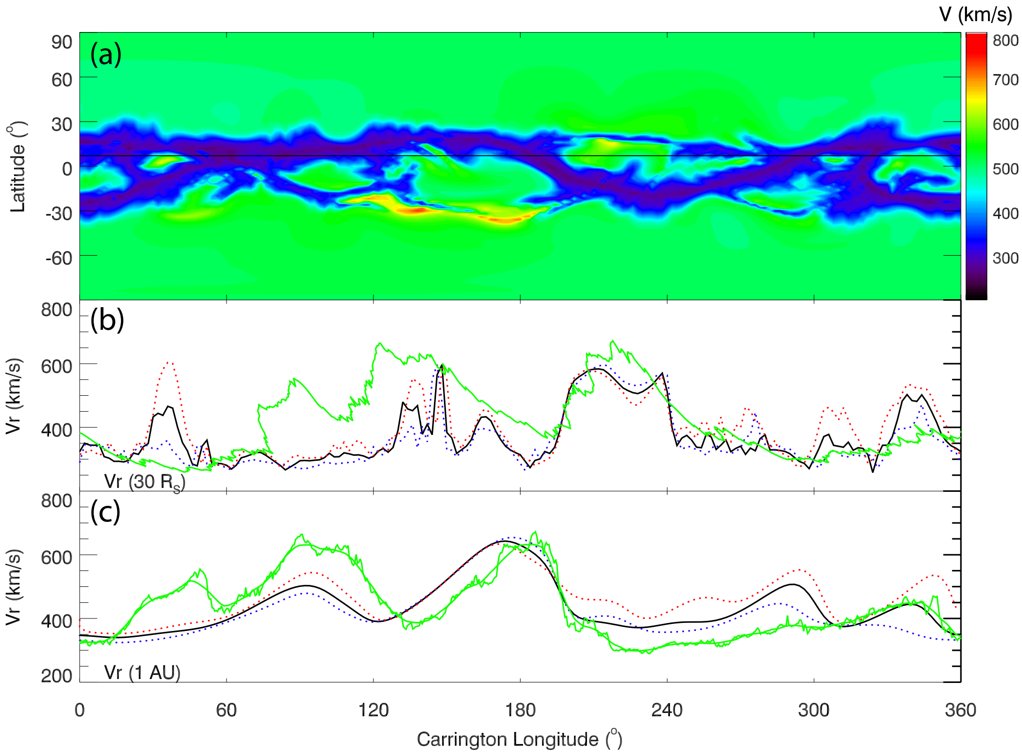

Figure 7. As Figure 5 but using the WSA model.

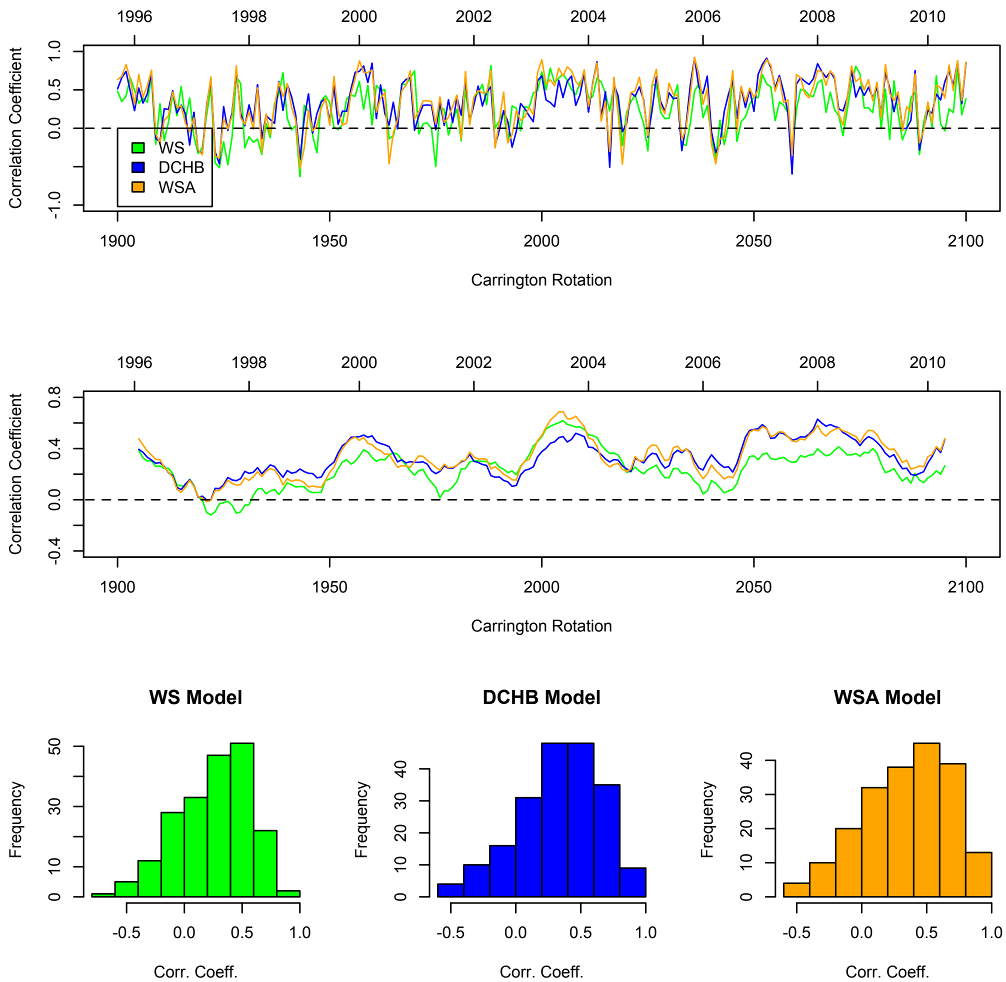

Figure 8. (a) Pearson correlation coefficients (PCCs) for the WS (green), DCHB (blue), and WSA (orange) as a function of Carrington rotation (or, equivalently, time) based on PFSS model solutions. (b) An 11-rotation running average of the PCCs. (c-e) Histograms of PCC for WS (c), DCHB (d), and WSA (e) models for the interval shown in (a) and (b).

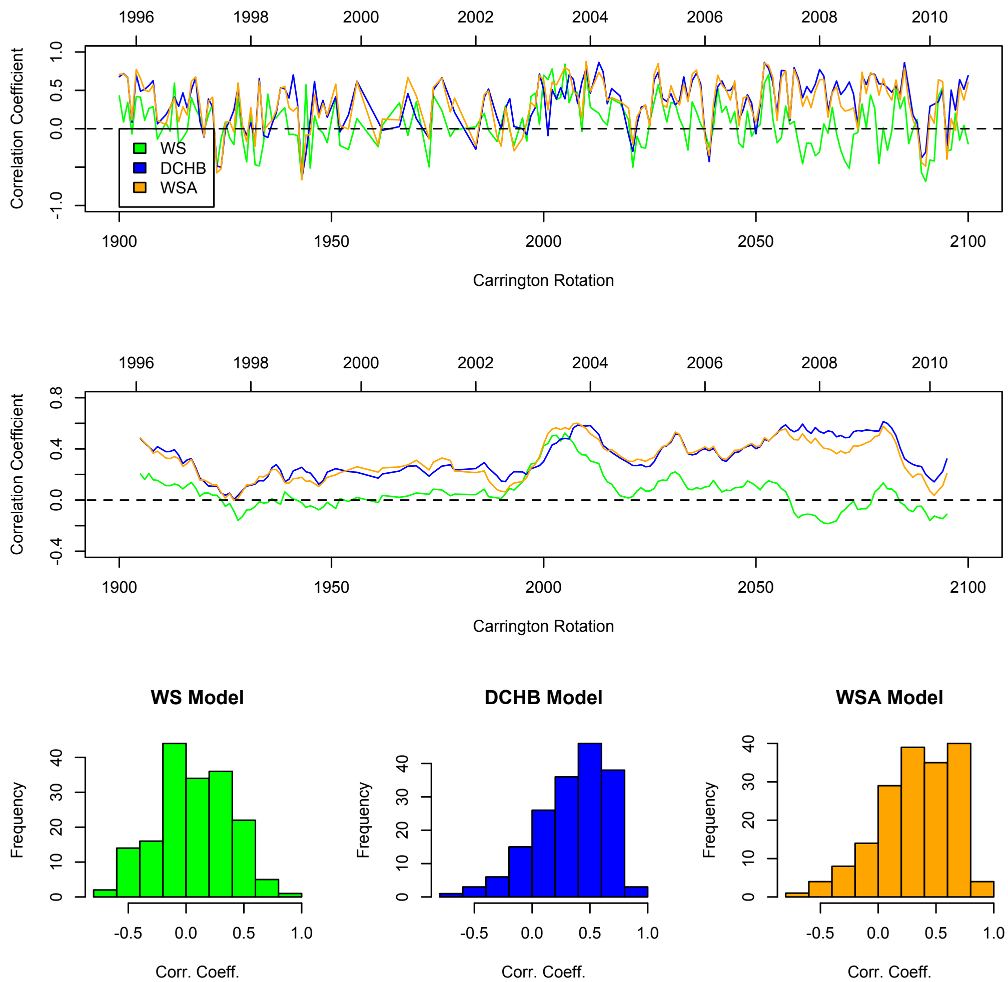

Figure 9. As Figure 9 but the speed maps are generated using MHD solutions.

Table 2. 'Optimum' parameters for WS, DCHB, and WSA models for selection of Carrington rotations.

Model	CR	V_{slow}	V_{fast}	α	ϵ	w	δ	ϕ	PCC
WS	1913	400.0	500.0	1.00				-0.0	0.648
WS	1928	200.0	500.0	1.00				11.5	0.708
WS	1936	266.7	500.0	1.00				-11.5	0.407
WS	1951	433.3	1000.0	1.00				-11.5	0.524
WS	1966	466.7	1000.0	1.00				11.5	0.604
WS	1979	400.0	722.2	1.00				-11.5	0.238
WS	1993	500.0	1000.0	1.00				11.5	0.242
WS	2008	300.0	666.7	1.00				0.0	0.597
WS	2023	433.3	500.0	1.00				11.5	0.025
WS	2038	200.0	611.1	1.00				-11.5	0.112
WS	2053	300.0	1000.0	1.00				11.5	0.789
WS	2060	500.0	1000.0	1.00				-11.5	-0.061
WS	2068	200.0	888.9	1.00				-11.5	0.445
WS	2083	200.0	1000.0	1.00				-0.0	0.634
DCHB	1913	240.0	400.0		0.04	0.01		-14.0	0.673
DCHB	1928	200.0	600.0		0.06	0.01		14.0	0.769
DCHB	1936	280.0	400.0		0.02	0.01		-14.0	0.439
DCHB	1951	200.0	400.0		0.06	0.01		-7.8	0.873
DCHB	1966	200.0	400.0		0.04	0.04		-14.0	0.513
DCHB	1979	200.0	600.0		0.05	0.01		1.5	0.358
DCHB	1993	360.0	400.0		0.02	0.01		-7.8	0.317
DCHB	2008	200.0	400.0		0.02	0.01		-7.8	0.623
DCHB	2023	360.0	400.0		0.02	0.01		-1.5	0.489
DCHB	2038	400.0	600.0		0.06	0.04		14.0	0.229
DCHB	2053	360.0	400.0		0.06	0.01		1.5	0.828
DCHB	2060	200.0	560.0		0.04	0.01		4.6	0.683
DCHB	2068	240.0	600.0		0.04	0.04		14.0	0.609
DCHB	2083	200.0	480.0		0.06	0.03		7.8	0.733
WSA	1913	200.0	550.0	0.40		0.40	5.00	-14.0	0.627
WSA	1928	200.0	750.0	0.30		0.22	5.00	7.8	0.697
WSA	1936	240.0	550.0	0.40		0.10	3.00	-14.0	0.451
WSA	1951	200.0	550.0	0.40		0.40	3.00	-14.0	0.777
WSA	1966	400.0	750.0	0.40		0.10	5.00	14.0	0.459
WSA	1979	400.0	670.0	0.38		0.22	4.20	-14.0	0.450
WSA	1993	400.0	750.0	0.40		0.40	3.00	14.0	0.171
WSA	2008	240.0	590.0	0.40		0.10	5.00	14.0	0.637
WSA	2023	200.0	550.0	0.40		0.10	5.00	-14.0	0.426
WSA	2038	360.0	750.0	0.30		0.16	5.00	14.0	0.338
WSA	2053	200.0	550.0	0.40		0.22	5.00	7.8	0.846
WSA	2060	200.0	750.0	0.30		0.34	5.00	-1.5	0.672
WSA	2068	400.0	750.0	0.30		0.40	5.00	-1.5	0.609
WSA	2083	200.0	550.0	0.30		0.22	5.00	4.6	0.706